Pore-scale study of dissolution-driven density instability with reaction $A + B \rightarrow C$ in porous media

Timan Lei and Kai H. Luo*
Department of Mechanical Engineering, University College London, Torrington Place, London WC1E 7JE, United Kingdom

(Received 23 December 2018; published 28 June 2019)

Dissolution-driven density instability (DI) occurs when a species A dissolves into a host fluid and introduces a buoyantly unstable stratification. Such an instability has positive effects in related applications and may be affected if species A reacts with solute B in the host fluid. In this paper, the lattice Boltzmann (LB) method is employed to simulate the dynamics of such an instability coupled with reaction $A + B \rightarrow C$ in porous media at the pore scale. Numerical simulations in homogeneous media have demonstrated that six types of dissolution-driven DI can be classified based on the Rayleigh numbers of three chemical species Ra_r (ratio of buoyancy to viscous forces), and reaction can accelerate, delay or even trigger the development of DI. Then, a parametric study has indicated that, increasing $\Delta\mathrm{Ra}_{CB}$ ($\mathrm{Ra}_C - \mathrm{Ra}_B$) can intensify density instability and reaction, promote the diffusion of species A, and also introduce either stabilizing or destabilizing effects of reaction. Besides, the increase of initial reactant concentration or/and Damköhler number Da (ratio of flow time to chemical time) can enhance the influence of chemistry. Finally, simulations are carried out in three types of heterogeneous media HE1–HE3, and six groups of fingering scenarios can also be observed in each medium. However, compared with the homogeneous case, heterogeneous media HE1 with randomly distributed solid grains can introduce deeper advancing position and rougher density fingering, and media HE2 and HE3 with vertical variations of pore spaces can affect the developing speed of fingering obviously. In terms of the storage of species A in the host fluid, medium HE2 with large pore size in the top layer is favorable. The present study is of significant importance for applications such as carbon capture and storage.

DOI: 10.1103/PhysRevFluids.4.063907

I. INTRODUCTION

Dissolution-driven DI in porous media develops when species A diffuses from above into a host fluid, leading to a buoyantly unstable stratification of the denser A-enriched fluid on top of the fresh host fluid [1]. This instability accompanied by convection can drive efficient mass and heat transport. It is thus at the heart of some natural and industrial processes, like groundwater management [2,3] and enhanced oil recovery [4]. It has also received considerable attention in the context of carbon dioxide (CO_2) sequestration, where convection is expected to improve the storage efficiency and security [5]. Moreover, dissolved species A can react with another solute B in the host fluid following the $A + B \rightarrow C$ scheme, and thereby modifying the density field and the fingering development [1]. It is therefore important to study the mechanisms of dissolution-driven DI coupled with reaction $A + B \rightarrow C$ in porous media, so as to provide design suggestions for relevant applications with respect to their expected instability behavior.

*k.luo@ucl.ac.uk

In recent years, experimental studies about dissolution-driven DI with chemical reactions have been performed in small reactors or Hele-Shaw cells. For instance, Budroni *et al.* [6] experimentally showed that the reaction between dissolved ester and alkaline hydroxides can delay the onset and the growth of density fingering and even introduce buoyantly stable stratifications. In parallel, experimental efforts were devoted to dissolution-driven DI in CO_2-alkaline solutions. Wylock *et al.* [7,8] observed both the well-developed and the suppressed density fingering in such a system by changing the solutes in alkaline solutions. Thomas *et al.* [9] and Cherezov *et al.* [10] then experimentally demonstrated that the reaction between dissolved CO_2 and alkaline hydroxides can accelerate density fingering, and the promotion intensity depends on the initial reactant concentrations. More recently, Budroni *et al.* [5] carried out experiments in ester-alkaline and CO_2-alkaline solutions separately. They showed that dissolution-driven DI can be either refrained or accelerated by chemical reactions.

The captured experimental results have confirmed the fact that chemical reaction can modify the fluid density and subsequently stabilize or destabilize dissolution-driven DI. The development of DI is often visualized by a pH color indicator because the solutions are transparent. It should be noted, however, that this technique may not always capture the whole extent of the convective dynamics [10,11]. In addition, the chemical influence intimately depends on the reactants, and existing experiments may not have covered all the scenarios. Therefore, theoretical investigations were performed to analyze dissolution-driven DI with reaction $A + B \rightarrow C$. For example, Kim *et al.* [12,13] studied the development of DI with chemical reaction in a porous medium using the linear stability theory. They pointed out that reaction can enhance, delay, or even introduce the fingering development. Loodts *et al.* [14–16] conducted a series of theoretical investigations to explore the chemical effects on dissolution-driven DI. They provided a classification of eight types of density profiles, with each one potentially representing a kind of DI dynamics.

Theoretical analyses have addressed the deficiencies in experimental investigations and predicted more reaction-induced scenarios of dissolution-driven DI. However, these predictions were based on fingering behavior in the early linear stage, and completely ignored the nonlinear fingering growth during the later period. Besides, theoretical results have not described the development details of density fingering, although they open the possibilities for chemical influence. For these reasons, numerical simulations have been conducted under the guidance of existing theoretical predictions. For instance, Kim *et al.* [12,13] numerically classified the chemical effects on dissolution-driven DI, employing their linear analysis results as initial conditions. Budroni *et al.* [5] numerically modeled both the stabilized and destabilized fingering phenomena and tested the effects of initial reactant concentrations. Their results qualitatively verified both experimental observations and theoretical predictions. In the meantime, Loodts *et al.* [1] numerically showed that reaction $A + B \rightarrow C$ can delay, accelerate, or trigger dissolution-driven DI, which matched well with their previous theoretical predictions. They provided the spatial-temporal dynamics of such an instability, including the species distributions, the dissolution of species A, and the reaction-rate distributions. In addition, they pointed out the difference between numerical and theoretical results when the development of DI reaches the later nonlinear stage.

In summary, numerical simulations have been proven to be capable of investigating dissolution-driven DI with chemical reactions more comprehensively. The existing numerical results have improved our understanding of this process and are of great importance in relevant industrial applications. However, two deficiencies in these numerical works should be noted. First, the medium heterogeneity is not considered. In the nonreactive case, the permeability anisotropy has been theoretically proven to be able of introducing considerable differences in fingering development [17], and this effect may be extended to the reactive case. Second, pore-scale simulations are still missing. Owing to the complex geometries in porous media, previous numerical studies were conducted on representative elementary volume (REV) scale, where a number of assumptions are required [18]. During the past three decades, the LB method has become an attractive alternative to conventional solvers for studying various fluid flow problems at pore scale [19,20]. This is attributed to its simple implementation, high parallelism, and ability to handle complex boundary conditions.

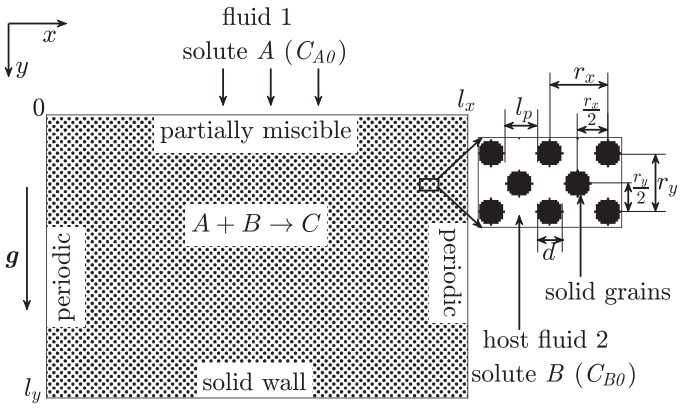

FIG. 1. The computational configuration.

Therefore, to fill the gaps in existing numerical investigations, the LB method is applied to simulate the dissolution-driven DI coupled with chemical reaction $A + B \rightarrow C$ in both homogeneous and heterogeneous media at pore scale.

II. MATHEMATICAL MODEL

In this study, dissolution-driven DI between two reactive solutions (labeled as 1 and 2) are investigated in two-dimensional (2D) porous media. Note that all the porous media in this work are generated artificially [21] and, unless stated otherwise, they share the same porosity ($\phi = 0.69$) and computational domain ($0 \leqslant x \leqslant l_x = 1, 0 \leqslant y \leqslant l_y = 2/3$), which allow for direct comparisons. As displayed in Fig. 1, fluid 1 that contains a solute A is placed upon a fluid-saturated porous medium, and host fluid 2 in pore spaces contains another dissolved reactant B. These two solutions, which are considered miscible and incompressible, are initially placed in contact along a horizontal interface at $y = 0$, with y pointing into fluid 2 along the gravity field. During the course of time, species A diffuses into the host fluid, and reacts with solute B to give a product C following the $A + B \rightarrow C$ scheme. The reaction rate R of this irreversible bimolecular reaction is taken as [1]

$$R = kC_AC_B, \tag{1}$$

with k being the kinetic reaction constant, and C_r being the concentration of species r ($r = A,\ B,\ C$). All three reactive species can thus contribute to changes in fluid density ρ. With the well-known Boussinesq approximation, ρ is considered as constant $\rho_0 = 1$ except in the body-force term, where it is assumed to vary linearly with local concentrations as [1]

$$\rho = \rho_0 + \rho_0(\beta_AC_A + \beta_BC_B + \beta_CC_C), \tag{2}$$

here β_r is the concentration expansion coefficient of species r.

In this work, the top boundary ($y = 0$) is assumed to be partially miscible [1]. Solute A can dissolve from fluid 1 into the host fluid, but no mass transfer takes place in the reverse direction. Thus, this work focuses on the dynamics in the host fluid, and the fluid motion and concentration evolutions can be described by the incompressible Navier-Stokes (NS) equations and the convection-diffusion-reaction (CDR) equations,

$$\nabla \cdot \boldsymbol{u} = 0, \tag{3}$$

$$\rho_0\left(\frac{\partial \boldsymbol{u}}{\partial t} + \boldsymbol{u} \cdot \nabla \boldsymbol{u}\right) = -\nabla p + \nabla \cdot (\nu\rho_0 \nabla \boldsymbol{u}) + \boldsymbol{F}, \tag{4}$$

$$\frac{\partial C_A}{\partial t} + \boldsymbol{u} \cdot \nabla C_A = D_A \nabla^2 C_A - R, \tag{5}$$

$$\frac{\partial C_B}{\partial t} + \boldsymbol{u} \cdot \nabla C_B = D_B \nabla^2 C_B - R, \tag{6}$$

$$\frac{\partial C_C}{\partial t} + \boldsymbol{u} \cdot \nabla C_C = D_C \nabla^2 C_C + R, \tag{7}$$

where $\boldsymbol{u} = (u,\ v)$ and p are the fluid velocity and pressure, respectively, t is the time, and ν is the kinematic viscosity. To avoid any double diffusive instabilities, the molecular diffusion coefficients D_r are set as constant D. The buoyancy term $\boldsymbol{F} = \rho \boldsymbol{g}$ is expressed as

$$\boldsymbol{F} = \rho_0 \boldsymbol{g}(\beta_A C_A + \beta_B C_B + \beta_C C_C), \tag{8}$$

with $\boldsymbol{g}$ being the acceleration vector of gravity. Note that the constant force term $\rho_0 \boldsymbol{g}$ has been absorbed into the pressure term ∇p in Eq. (4) [22]. The present governing equations (3)–(7) can be solved with the initial conditions

$$\begin{aligned} &C_A(x,\ 0 \leqslant y \leqslant \vartheta,\ 0) = C_{A0} = 1, \quad C_A(x,\ y > \vartheta,\ 0) = 0, \\ &C_B(x,\ y,\ 0) = C_{B0}, \quad C_C(x,\ y,\ 0) = 0. \end{aligned} \tag{9}$$

Note that the concentration of species A at the top boundary ($y = 0$) is initially considered to be equal to its solubility C_{A0} in fluid 2, and this value remains constant over time following the local chemical equilibrium assumption [1]. It should be emphasized that, in order to trigger density instability, a small perturbation ϑ is introduced in the initial concentration distribution of species A near the top boundary. The value of ϑ randomly varies along the x direction within the range $[0,\ 0.0067 l_x]$. The boundary conditions are also required and, as displayed in Fig. 1, the periodic boundary conditions in velocity and concentration are applied for all chemical species at the lateral boundaries ($x = 0$, $x = l_x$). The no-slip and no-flux boundary conditions are used for all species at the solid matrix interface [$\boldsymbol{x} = (x_s,\ y_s)$], the solid bottom wall ($y = l_y$), and the top boundary ($y = 0$), except for the no-slip and prescribed concentration for species A at the partially miscible top interface ($y = 0$). These boundary conditions can be described by

$$\begin{aligned} C_r(0,\ y,\ t) &= C_r(l_x,\ y,\ t), \quad \boldsymbol{u}(0,\ y,\ t) = \boldsymbol{u}(l_x,\ y,\ t), \\ \nabla C_r(x,\ l_y,\ t) &= (0,\ 0), \quad \boldsymbol{u}(x,\ l_y,\ t) = (0,\ 0), \\ C_A(x,\ 0,\ t) &= C_{A0}, \quad \nabla C_{B,C}(x,\ 0,\ t) = (0,\ 0), \quad \boldsymbol{u}(x,\ 0,\ t) = (0,\ 0), \\ \nabla C_r(x_s,\ y_s,\ t) &= (0,\ 0), \quad \boldsymbol{u}(x_s,\ y_s,\ t) = (0,\ 0). \end{aligned} \tag{10}$$

Equations (3)–(7) can be expressed in a dimensionless form by introducing the characteristic length L, velocity U, time T, and concentration C_d as

$$L = l_x, \quad U = \sqrt{g \beta_A L C_{A0}}, \quad T = L/U, \quad C_d = C_{A0}. \tag{11}$$

In terms of the following nondimensional variables,

$$\begin{aligned} &\boldsymbol{u}^* = \frac{\boldsymbol{u}}{U}, \quad p^* = \frac{p}{\rho_0 U^2}, \quad C_r^* = \frac{C_r}{C_{A0}}, \quad \eta = \frac{C_{B0}}{C_{A0}}, \\ &x^* = \frac{x}{L}, \quad y^* = \frac{y}{L}, \quad t^* = \frac{t}{T}, \quad \rho^* = \frac{\rho - \rho_0}{\rho_0 \beta_A C_{A0}}, \quad \boldsymbol{F}^* = \frac{\boldsymbol{F}}{\rho_0 U^2 / L}, \\ &R^* = \mathrm{Da} C_A^* C_B^*, \quad \mathrm{Ra}_r = \frac{g \beta_r C_{A0} L^3}{\nu D}, \quad \mathrm{Sc} = \frac{\nu}{D}, \quad \mathrm{Da} = \frac{k C_{A0} L}{U}, \end{aligned} \tag{12}$$

where the asterisked variables are the corresponding dimensionless ones, the dimensionless equations (3)–(7) read

$$\nabla \cdot \boldsymbol{u}^* = 0, \tag{13}$$

$$\frac{\partial \boldsymbol{u}^*}{\partial t^*} + \boldsymbol{u}^* \cdot \nabla \boldsymbol{u}^* = -\nabla p^* + \sqrt{\frac{\mathrm{Sc}}{\mathrm{Ra}_A}} \nabla \cdot (\nu \nabla \boldsymbol{u}^*) + \boldsymbol{F}^*, \tag{14}$$

$$\frac{\partial C_A^*}{\partial t^*} + \boldsymbol{u}^* \cdot \nabla C_A^* = \frac{1}{\sqrt{\mathrm{Ra}_A \mathrm{Sc}}} \nabla^2 C_A^* - R^*, \tag{15}$$

$$\frac{\partial C_B^*}{\partial t^*} + \boldsymbol{u}^* \cdot \nabla C_B^* = \frac{1}{\sqrt{\mathrm{Ra}_A \mathrm{Sc}}} \nabla^2 C_B^* - R^*, \tag{16}$$

$$\frac{\partial C_C^*}{\partial t^*} + \boldsymbol{u}^* \cdot \nabla C_C^* = \frac{1}{\sqrt{\mathrm{Ra}_A \mathrm{Sc}}} \nabla^2 C_C^* + R^*. \tag{17}$$

Note that, by adding Eqs. (16) and (17) and taking into account the initial and boundary conditions in Eqs. (9) and (10), the concentration of species B and C can be expected to remain constant because $C_B + C_C = C_{B0}$. Based on this relationship, the dimensional force term can be rewritten as

$$\boldsymbol{F}^* = \frac{\boldsymbol{F}}{\rho_0 U^2 / L} = \left(C_A^* + \frac{\Delta \mathrm{Ra}_{CB}}{\mathrm{Ra}_A} C_B^* + \frac{\mathrm{Ra}_B}{\mathrm{Ra}_A} \eta \right) \boldsymbol{j}, \tag{18}$$

with $\Delta \mathrm{Ra}_{CB} = \mathrm{Ra}_C - \mathrm{Ra}_B$ representing the relative contribution to the density of product C and reactant B. Therefore, the behavior of the dissolution-driven DI with reaction $A + B \rightarrow C$ is characterized by the Rayleigh numbers Ra_r, the Schmidt number Sc, the Damköhler number Da, and the initial concentration ratio η.

III. NUMERICAL METHOD

In this work, the multiple-relaxation time (MRT) LB model [18,23,24] is employed to solve the above governing equations (3)–(7). This model can avoid the unphysical dependence of permeability on viscosity for pore-scale simulations. Specifically, the most popular two-dimensional nine-velocity (D2Q9) LB model is applied, and the corresponding discrete velocities $\boldsymbol{e}_i$ and weight coefficients w_i are defined as [18]

$$\begin{aligned}
&\boldsymbol{e}_i = e(0,\ 0), && w_i = \frac{4}{9}, && i = 0 \\
&\boldsymbol{e}_i = e\left(\cos\frac{(i-1)\pi}{2}, \sin\frac{(i-1)\pi}{2} \right), && w_i = \frac{1}{9}, && i = 1-4 \\
&\boldsymbol{e}_i = \sqrt{2} e\left(\cos\frac{(2i-1)\pi}{4}, \sin\frac{(2i-1)\pi}{4} \right), && w_i = \frac{1}{36}, && i = 5-8,
\end{aligned} \tag{19}$$

where $e = \delta_x / \delta_t$ is the lattice speed, with δ_x and δ_t denoting the lattice spacing and the time step, respectively. In the following simulations, the parameter e is set as $e = 1$.

The present model consists of four LB equations, with one for the NS equations and three for the CDR equations. Since the LB equations for concentration transport of species A, B, and C are of the same pattern, only one of them is introduced here. The evolution equations of the D2Q9 MRT LB model for the NS equations (3) and (4) and the CDR equation (5) of species A are [18,24]

$$f_i(\boldsymbol{x} + \boldsymbol{e}_i \delta_t,\ t + \delta_t) - f_i(\boldsymbol{x},\ t) = -(\boldsymbol{M}^{-1} \boldsymbol{S} \boldsymbol{M})_{ij} \left[f_j(\boldsymbol{x},\ t) - f_j^{\mathrm{eq}}(\boldsymbol{x},\ t) \right] + \delta_t \left[\boldsymbol{M}^{-1} \left(\boldsymbol{I} - \frac{\boldsymbol{S}}{2} \right) \boldsymbol{M} \right]_{ij} \bar{F}_j, \tag{20}$$

$$g_i(\boldsymbol{x} + \boldsymbol{e}_i \delta_t,\ t + \delta_t) - g_i(\boldsymbol{x},\ t) = -(\boldsymbol{M}^{-1} \boldsymbol{S}' \boldsymbol{M})_{ij} \left[g_j(\boldsymbol{x},\ t) - g_j^{\mathrm{eq}}(\boldsymbol{x},\ t) \right] + \delta_t \bar{R}_i + \frac{\delta_t^2}{2} \partial_t \bar{R}_i, \tag{21}$$

for $i,\ j = 0,\ 1, \ldots, 8$, where $f_i(\boldsymbol{x},\ t)$ and $g_i(\boldsymbol{x}, t)$ are the distribution functions for the hydrodynamics and the concentration fields, respectively. To recover the incompressible NS equations correctly, the equilibrium distribution functions f_i^{eq} and g_i^{eq} are given as [18]

$$f_i^{\mathrm{eq}} = w_i\left[\rho_p + \rho_0\left(\frac{\boldsymbol{e}_i\cdot\boldsymbol{u}}{c_s^2} + \frac{\boldsymbol{uu}:\left(\boldsymbol{e}_i\boldsymbol{e}_i - c_s^2\boldsymbol{I}\right)}{2c_s^4}\right)\right], \tag{22}$$

$$g_i^{\mathrm{eq}} = w_i C_A\left[1 + \frac{\boldsymbol{e}_i\cdot\boldsymbol{u}}{c_s^2} + \frac{\boldsymbol{uu}:\left(\boldsymbol{e}_i\boldsymbol{e}_i - c_s^2\boldsymbol{I}\right)}{2c_s^4}\right]. \tag{23}$$

Here ρ_p is a variable related to the fluid pressure as $p = c_s^2\rho_p$, with $c_s = e/\sqrt{3}$ being the lattice sound velocity. To avoid discrete lattice effects in the LB model, the forcing and reactive distribution functions $\bar{F}_i$ and $\bar{R}_i$ are [18,20]

$$\bar{F}_i = w_i\left[\frac{\boldsymbol{e}_i\cdot\boldsymbol{F}}{c_s^2} + \frac{\boldsymbol{uF}:\left(\boldsymbol{e}_i\boldsymbol{e}_i - c_s^2\boldsymbol{I}\right)}{c_s^4}\right], \tag{24}$$

$$\bar{R}_i = w_i R\left(1 + \frac{\boldsymbol{e}_i\cdot\boldsymbol{u}}{c_s^2}\frac{\tau_c - 0.5}{\tau_c}\right). \tag{25}$$

The time derivative term in Eq. (21) is treated by the backward scheme as $\partial_t\bar{R}_i(\boldsymbol{x},\ t) = [\bar{R}_i(\boldsymbol{x},\ t) - \bar{R}_i(\boldsymbol{x},\ t - \delta_t)]$. The transformation matrix $\boldsymbol{M}$ is

$$\boldsymbol{M} = \begin{pmatrix} 1 & 1 & 1 & 1 & 1 & 1 & 1 & 1 & 1 \\ -4 & -1 & -1 & -1 & -1 & 2 & 2 & 2 & 2 \\ 4 & -2 & -2 & -2 & -2 & 1 & 1 & 1 & 1 \\ 0 & 1 & 0 & -1 & 0 & 1 & -1 & -1 & 1 \\ 0 & -2 & 0 & 2 & 0 & 1 & -1 & -1 & 1 \\ 0 & 0 & 1 & 0 & -1 & 1 & 1 & -1 & -1 \\ 0 & 0 & -2 & 0 & 2 & 1 & 1 & -1 & -1 \\ 0 & 1 & -1 & 1 & -1 & 0 & 0 & 0 & 0 \\ 0 & 0 & 0 & 0 & 0 & 1 & -1 & 1 & -1 \end{pmatrix}. \tag{26}$$

This matrix can map the distribution functions from the physical space $\boldsymbol{\psi} = (\psi_0,\ \psi_1,\ \psi_2, \ldots, \psi_8)^{\mathrm{T}}$ to the moment space as $\hat{\boldsymbol{\psi}} = \boldsymbol{M}\cdot\boldsymbol{\psi}$. With this transformation, the evolution equations (20) and (21) can be implemented in the moment space as

$$\hat{\boldsymbol{f}}(\boldsymbol{x} + \boldsymbol{e}_i\delta_t,\ t + \delta_t) = \hat{\boldsymbol{f}}(\boldsymbol{x},\ t) - \boldsymbol{S}[\hat{\boldsymbol{f}}(\boldsymbol{x},\ t) - \hat{\boldsymbol{f}}^{\mathrm{eq}}(\boldsymbol{x},\ t)] + \delta_t\left(\boldsymbol{I} - \frac{\boldsymbol{S}}{2}\right)\hat{\boldsymbol{F}}, \tag{27}$$

$$\hat{\boldsymbol{g}}(\boldsymbol{x} + \boldsymbol{e}_i\delta_t,\ t + \delta_t) = \hat{\boldsymbol{g}}(\boldsymbol{x},\ t) - \boldsymbol{S}'[\hat{\boldsymbol{g}}(\boldsymbol{x},\ t) - \hat{\boldsymbol{g}}^{\mathrm{eq}}(\boldsymbol{x},\ t)] + \delta_t\hat{\boldsymbol{R}} + \frac{\delta_t^2}{2}\partial_t\hat{\boldsymbol{R}}, \tag{28}$$

where $\boldsymbol{S}$ and $\boldsymbol{S}'$ are the diagonal relaxation matrix of relaxation rates s_i and s_i' in the moment space, respectively. In the following simulations, the relaxation rates are chosen as used in Refs. [24,25]. The equilibrium moments $\hat{\boldsymbol{f}}^{\mathrm{eq}}$ and $\hat{\boldsymbol{g}}^{\mathrm{eq}}$ are defined by

$$\hat{\boldsymbol{f}}^{\mathrm{eq}} = (\rho_p,\ -2\rho_p + 3\rho_0\boldsymbol{u}^2,\ \rho_p - 3\rho_0\boldsymbol{u}^2,\ \rho_0 u,\ -\rho_0 u, \rho_0 v,\ -\rho_0 v,\ \rho_0(u^2 - v^2),\ \rho_0 uv), \tag{29}$$

$$\hat{\boldsymbol{g}}^{\mathrm{eq}} = (C_A,\ C_A(-2 + 3\boldsymbol{u}^2), C_A(1 - 3\boldsymbol{u}^2),\ C_A u,\ -C_A u,\ C_A v,\ -C_A v,\ C_A(u^2 - v^2),\ C_A uv), \tag{30}$$

and the corresponding forcing and reactive moments are expressed as

$$\hat{\boldsymbol{F}} = (0,\ 6\boldsymbol{u}\cdot\boldsymbol{F},\ -6\boldsymbol{u}\cdot\boldsymbol{F},\ F_x,\ -F_x,\ F_y,\ -F_y,\ 2(uF_x - vF_y),\ (uF_y + vF_x)), \tag{31}$$

$$\hat{\boldsymbol{R}} = \left(R,\ -2R,\ R,\ \left(1-\frac{s_3'}{2}\right)uR,\ -\left(1-\frac{s_4'}{2}\right)uR,\ \left(1-\frac{s_5'}{2}\right)vR,\ -\left(1-\frac{s_6'}{2}\right)vR,\ 0,\ 0\right). \tag{32}$$

Finally, the macroscopic variables can be obtained from the distribution functions as

$$\rho_p = \sum_i f_i, \quad \rho_0\boldsymbol{u} = \sum_i \boldsymbol{e}_i f_i + \frac{\delta_t}{2}\boldsymbol{F}, \quad C_A = \sum_i g_i. \tag{33}$$

Note that the present model is similar to the one proposed in Ref. [24], except for the exclusion of the lattice kinetic scheme and the inclusion of three reactive species. Through the Chapman-Enskog analysis on the present LB equations, the governing equations (3)–(7) can be recovered with the relaxation times τ and τ_c being

$$\nu = c_s^2\left(\tau - \tfrac{1}{2}\right)\delta_t, \quad D = c_s^2\left(\tau_c - \tfrac{1}{2}\right)\delta_t. \tag{34}$$

Besides, the present model has been extensively validated as in Ref. [24], and the details are not included for brevity. Therefore, it is employed for the following pore-scale studies of the dissolution-driven DI coupled with reaction $A + B \to C$. During the LB simulations, the treatment of boundary conditions in Eq. (10) also plays an important role. In this work, the no-slip velocity and impermeable concentration conditions at the bottom solid wall and the porous matrix interface are realized by the halfway bounce-back scheme [26,27], and the partially miscible condition at the top boundary is treated with the nonequilibrium extrapolation scheme [18].

IV. RESULTS AND DISCUSSION

In this section, dissolution-driven DI with reaction $A + B \to C$ is simulated in both homogeneous and heterogeneous porous media based on the above LB method. Specifically, this work focuses on the interaction between reaction and density fingering, thus the Schmidt number is fixed as $\mathrm{Sc} = 100$, and different values of Ra_r, Da, and η are selected to change the test conditions. In addition, the characteristic parameters in Eq. (11) are set as

$$L = l_x = 1, \quad U = \sqrt{g\beta_A L C_{A0}} = 0.177, \quad T = L/U = 5.65, \quad C_d = C_{A0} = 1, \tag{35}$$

and they are all in lattice units. Based on these characteristic numbers, the relevant parameters in LB simulations can be calculated as

$$\begin{aligned} \nu &= \frac{LU}{\sqrt{\mathrm{Ra}_A/\mathrm{Sc}}}, \quad D = \frac{LU}{\sqrt{\mathrm{Ra}_A\mathrm{Sc}}}, \quad C_{B0} = C_{A0}\eta, \\ \tau &= \frac{\nu}{c_s^2\delta_t} + \frac{1}{2}, \quad \tau_c = \frac{D}{c_s^2\delta_t} + \frac{1}{2}, \quad k = \frac{U\mathrm{Da}}{LC_{A0}}. \end{aligned} \tag{36}$$

Before proceeding further, grid convergence tests have been carried out for all the porous media involved in this work, and a mesh of size $N_x \times N_y = 1500 \times 1000$ is chosen for the subsequent simulations, unless otherwise noted.

A. General phenomena

The general phenomena of dissolution-driven DI coupled with reaction $A + B \to C$ are first investigated in a homogeneous porous medium HO. As displayed in Fig. 1, the porous network contains a staggered array of circular grains with a uniform diameter $d = 12\delta_x$, where the lattice spacing is $\delta_x = l_x/N_x$. Every grain center $G_{\mathrm{HO}} = (x_c,\ y_c)$ locates on a grid node and obeys a regular staggered distribution. The closest center-to-center distances between two cylinders in the x and

TABLE I. Parameters for Tests NR and R1–R3.

Tests	Parameters
NR	$\mathrm{Ra}_A = 10^9, \quad \mathrm{Da} = 0, \quad \eta = 0$
R1	$\mathrm{Ra}_A = 10^9, \quad \Delta\mathrm{Ra}_{CB} = -10^9, \quad \mathrm{Da} = 5, \quad \eta = 1$
R2	$\mathrm{Ra}_A = 10^9, \quad \Delta\mathrm{Ra}_{CB} = 10^9, \quad \mathrm{Da} = 5, \quad \eta = 1$
R3	$\mathrm{Ra}_A = -10^9, \quad \Delta\mathrm{Ra}_{CB} = 10^9, \quad \mathrm{Da} = 5, \quad \eta = 1$

y directions are $r_x = 27\delta_x$ and $r_y = 27\delta_x$, respectively, and the single pore size can be calculated as $l_p = r_x - d = 15\delta_x$. After a series of simulations and comparisons, the development of DI can be divided into two nonreactive and four reactive groups, based on the Rayleigh numbers Ra_r of chemical species. To be specific, these six groups can be described as follows:

(I) For $\mathrm{Ra}_A > 0$, nonreactive unstable.

(1) Nonreactive group NR: The dissolution of species A into the host fluid is buoyantly unstable and can trigger dissolution-driven DI.

(2) Reactive group R1: Reaction can suppress the development of dissolution-driven DI with species C being lighter than B ($\Delta\mathrm{Ra}_{CB} < 0$).

(3) Reactive group R2: Reaction can enhance the development of dissolution-driven DI provided C is sufficiently denser than B ($\Delta\mathrm{Ra}_{CB} > 0$).

(II) For $\mathrm{Ra}_A < 0$, nonreactive stable.

(4) Nonreactive group NRS: The dissolution of species A into the host fluid is buoyantly stable.

(5) Reactive group R3: Reaction can create an unstable density stratification and trigger the development of DI with $\Delta\mathrm{Ra}_{CB} > 0$.

(6) Reactive group R4: The system with reaction remains stable under the condition $\Delta\mathrm{Ra}_{CB} < 0$.

This classification is similar to existing predictions by linear stability analysis in Ref. [15], with the double diffusive instability not being included. As an example, a few specific test conditions are provided in Table I to investigate the general phenomena, including one nonreactive Test NR, and three reactive Tests R1–R3. Note that the nonreactive group NRS and the reactive group R4 are not included because no fingering develops in these stable systems. Figure 2 depicts the numerical density distributions varying with time for Tests NR and R1–R3, which can reflect the typical characteristics of DI in different groups.

The results show that the general dynamics of dissolution-driven DI in each test follows four similar stages. Initially, the miscible interface between A-enriched fluid and fresh host fluid maintains nearly as a plane [Fig. 2(a)], and diffusion dominates the flow dynamics in this short period. Then the interface deforms gradually with the diffusion of species A, and fingers of denser fluid appear and sink into the host fluid [Fig. 2(b)]. After that, fingers begin to interact and merge with their neighbors, and the number of fingers decreases dramatically [Figs. 2(c) and 2(d)]. Finally, small new fingers regenerate from the top boundary and join the existing ones, and the number of fingers remains almost unchanged [Figs. 2(e) and 2(f)].

Together with these similarities, differences between fingering behavior in Tests NR and R1–R3 are obvious as well. This is explained with the help of horizontally averaged density $\bar{\rho}^*$ in Fig. 3. In Test NR, density fingering develops gradually with the dissolution of A [Fig. 2, column (1)], and the density profile at each time instance decreases monotonically [Fig. 3(a)]. Compared with this nonreactive case, dissolution-driven DI coupled with reaction $A + B \rightarrow C$ develops more slowly in Test R1 [Fig. 2, column (2)]. This is because product C cannot compensate the consumption of reactant B in terms of density evolution ($\Delta\mathrm{Ra}_{CB} < 0$), and a density profile with a minimum builds up at every time instant [Fig. 3(b)]. It is observed that each density curve decreases vertically to the minimum in the upper part and returns to increase from the minimum in the lower part [Fig. 3(b)].

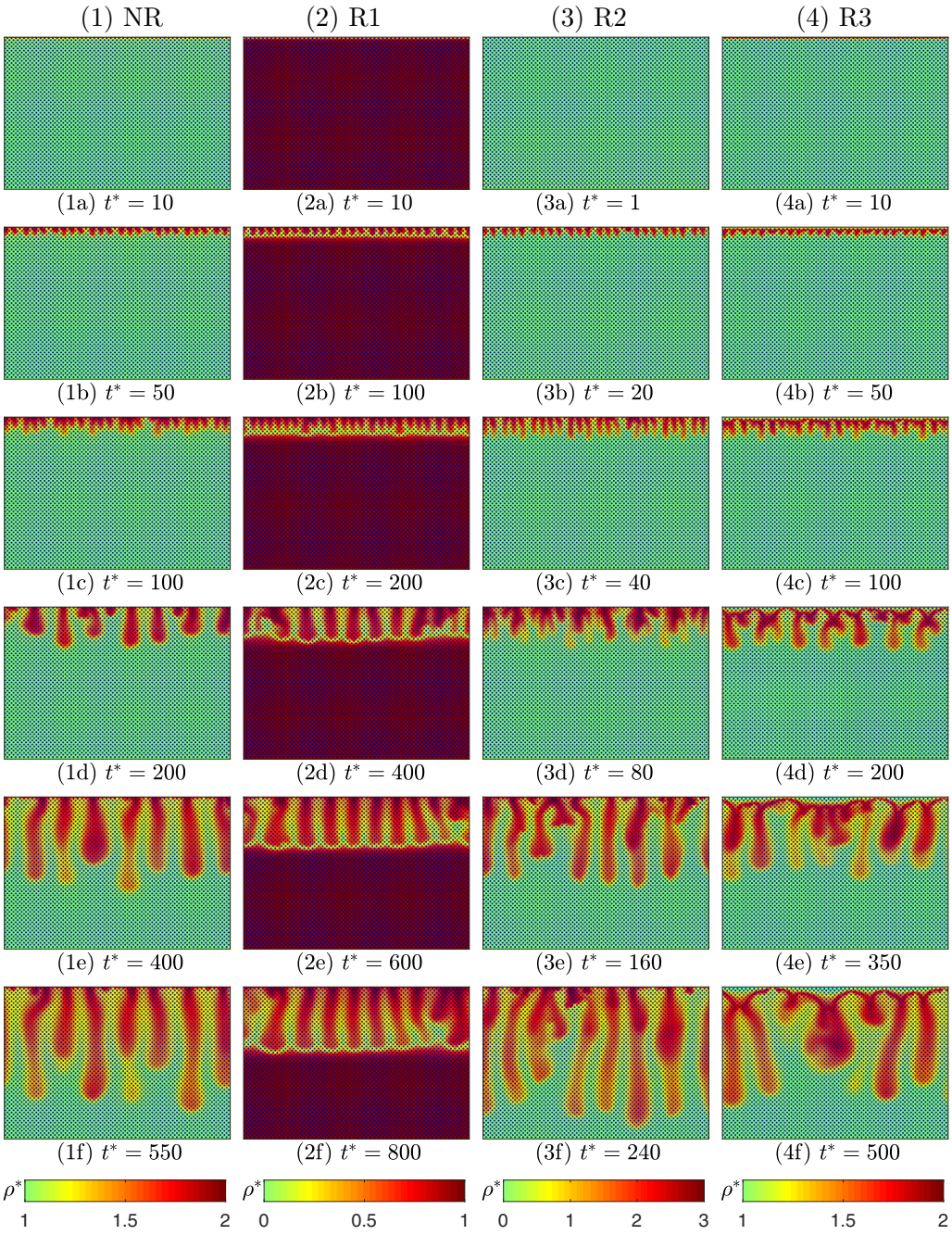

FIG. 2. Density fields for Tests NR and R1–R3 in homogeneous medium HO.

Dissolution-driven DI thus only develops in the upper unstable stratification, and the lower stable layer acts as a barrier to counteract the fingering growth. Note that, compared with previous REV-scale density profiles [1], the width of the present pore-scale minimum also enlarges progressively with time, while no transition from a strict local minimum to a zone with $\bar{\rho}^*$ being constant as the minimum occurs. For pore- and REV-scale simulations, Tartakovsky *et al.* [28,29] have argued

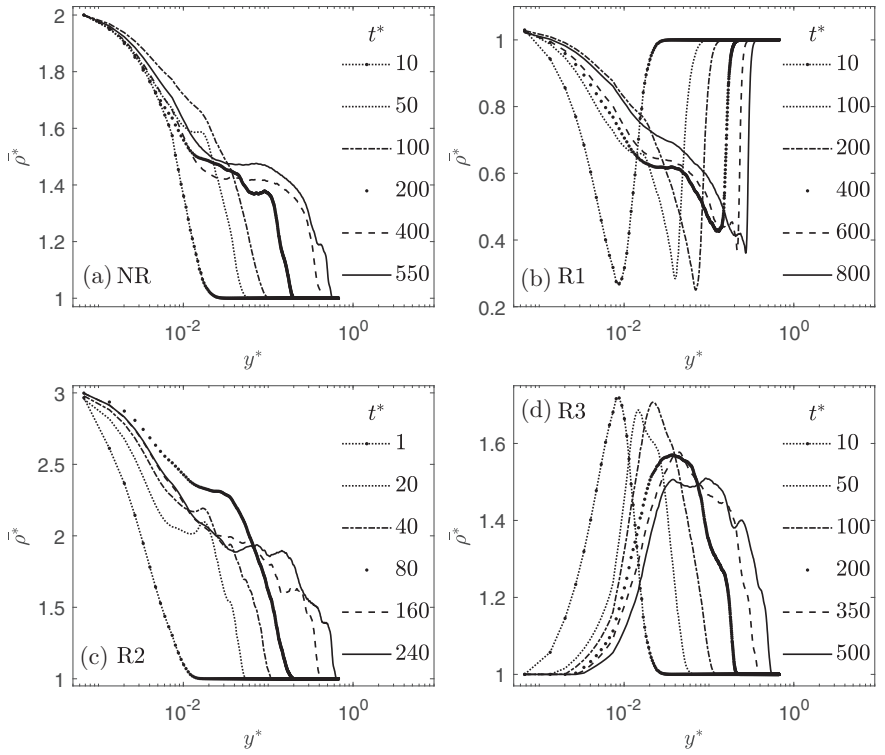

FIG. 3. Horizontally averaged density profiles for Tests NR and R1–R3 in homogeneous medium HO.

that the REV-scale flow and transport equations can be obtained by averaging the corresponding pore-scale ones over a support volume, but the use of effective dispersion and permeability models at REV scale tends to overpredict the degree of mixing and reaction. In addition, they simulated the transport of two solutes A and B coupled with reaction $A + B \rightarrow C$ in porous media on both REV and pore scales. Their results revealed that, the REV-scale model overestimated the global (also global-averaged) mass of product C, implying the overestimated reaction rate between solutes A and B on REV scale. This finding can be applied to explain the inconsistency between the present pore-scale and previous REV-scale results. That is, REV-scale simulations may have over-predicted the extent of reaction and introduced the largest reaction (minimum density) over a certain depth.

By contrast, density fingering appears earlier and elongates more rapidly in reactive Test R2 [Fig. 2, column (3)] than that in nonreactive Test NR [Fig. 2, column (1)]. This can be expected since the contribution to density of product C is sufficiently larger than reactant B ($\Delta \mathrm{Ra}_{CB} > 0$). Under this condition, every density profile in Fig. 3(c) decreases monotonically along y as in Test NR. But product C enlarges the density difference from top ($y = 0$) to bottom ($y = l_y$) and subsequently enhances the fingering growth. Similarly, in Test R3, dissolution-driven DI develops due to the inclusion of reaction $A + B \rightarrow C$ with $\Delta \mathrm{Ra}_{CB} > 0$ [Fig. 2, column (4)], even its nonreactive counterpart is stable. The density profiles in this test show a nonmonotonic fashion [Fig. 3(d)] as in Test R1 [Fig. 3(b)], and each curve has a reaction-induced maximum. Density fingering develops in the lower unstable part, while the upper stable stratification corresponds to the narrow stagnant liquid layer near the top boundary [Fig. 2, column (4)].

Generally, in agreement with previous theoretical predictions [15], six kinds of fingering scenarios can be classified from the present pore-scale simulations. Each case has a specific type of density profile, and the nonmonotonic one appears when Ra_A and $\Delta \mathrm{Ra}_{CB}$ have the opposite signs. However, density profiles in Fig. 3 fluctuate at later time instances due to the nonlinear

TABLE II. Parameters for Tests I–IV.

Tests	Parameters ($\mathrm{Ra}_A = 10^9$)
I	$\Delta\mathrm{Ra}_{CB}/\mathrm{Ra}_A = -1,\ 0,\ 0.25,\ 0.5,\ 0.75,\ 1;\quad \mathrm{Da} = 5;\quad \eta = 1$
II	$\eta = 0.1,\ 0.5,\ 1,\ 1.5,\ 2;\quad \Delta\mathrm{Ra}_{CB} = 10^9;\quad \mathrm{Da} = 5$
III	$\mathrm{Da} = 1,\ 5,\ 10,\ 50,\ 100;\quad \Delta\mathrm{Ra}_{CB} = 10^9;\quad \eta = 1$
IV	$\Delta\mathrm{Ra}_{CB}/\mathrm{Ra}_A = 0.25,\ 0.35,\ 0.4,\ 0.5;\quad \mathrm{Da} = 5;\quad \eta = 1$

fingering development, which cannot be theoretically predicted by linear stability analysis [15]. In addition, compared with existing REV-scale investigations [1], the present simulations can also qualitatively reproduce the fact that reaction $A + B \rightarrow C$ can stabilize (Test R1), destabilize (Test R2) or even trigger (Test R3) dissolution-driven DI. On the other hand, different from previous REV-scale density profiles, no plateau with $\bar{\rho}^*$ remaining constant as a minimum exists in the present pore-scale ones (Fig. 3), and this can be explained by the overprediction of reaction extent at REV scale. Therefore, the present pore-scale results can clarify more progression details.

B. Parametric study

After the observation of general phenomena, a parametric study is further carried out in homogeneous medium HO. As summarized in Table II, Tests I–III are performed to evaluate the relationship between dissolution-driven DI and reaction $A + B \rightarrow C$, with different values of $\Delta\mathrm{Ra}_{CB}$, η, and Da. Note that, Test I with fixed Ra_A and varying $\Delta\mathrm{Ra}_{CB}$ can represent different pairs of reactants A, B and product C.

The quantity l_m is defined as the most advanced vertical position of fingering tips, and it represents the extension zone of dissolution-driven DI. Time evolutions of l_m for Test I are displayed in Fig. 4, and the corresponding nonreactive result is included for comparison. It is shown that l_m for each $\Delta\mathrm{Ra}_{CB}$ matches well in the early stage, when diffusion dominates the fluid dynamics [Fig. 2(a)]. After a short period t_s, l_m start to depart from the initial diffusive trend and increase faster. This is because the unstable stratification becomes more intensive with the diffusion of species A, and density fingering starts at t_s [Fig. 2(b)]. The time period t_s decreases monotonically as $\Delta\mathrm{Ra}_{CB}$ increases, which implies the increasing destabilizing effects of chemistry. Besides, a critical value $\Delta\mathrm{Ra}_{CB1} = 0.25\mathrm{Ra}_A$ can be observed, above which the reactive l_m deviates from

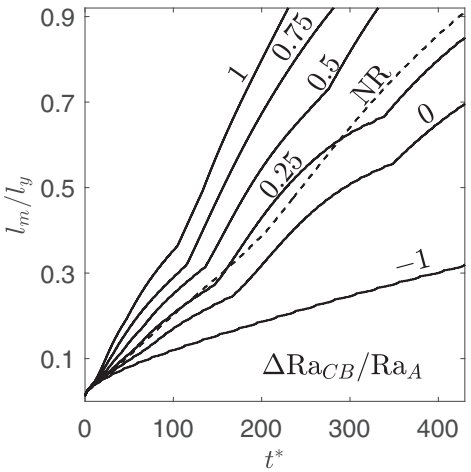

FIG. 4. Time evolutions of the mixing length for Test I in homogeneous medium HO.

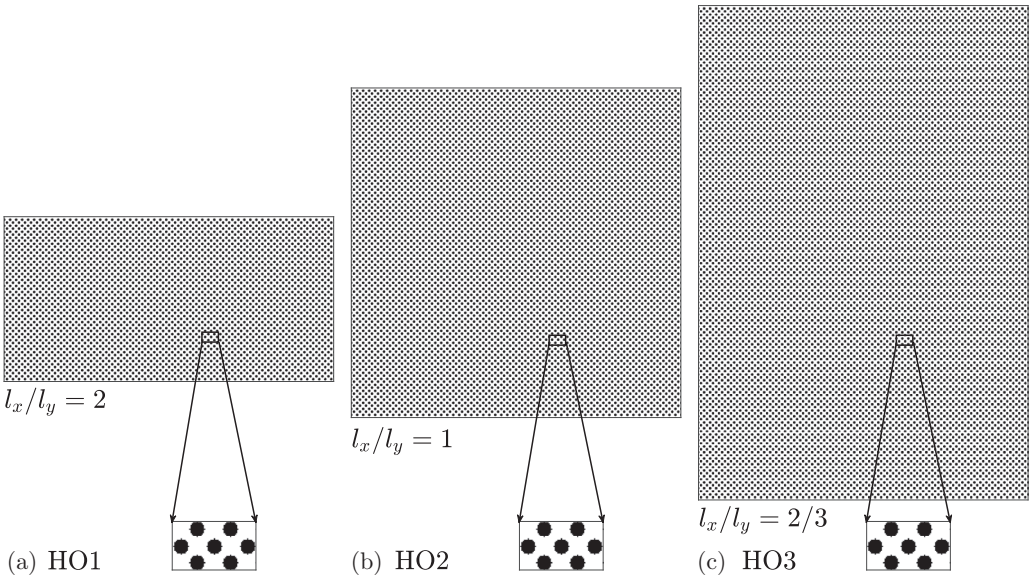

FIG. 5. Schematic diagram of homogeneous media HO1–HO3 with different aspect ratios.

the diffusion stage earlier than the nonreactive one. On the basis of this property, the chemical stabilizing ($\Delta\mathrm{Ra}_{CB} < \Delta\mathrm{Ra}_{CB1}$) and destabilizing ($\Delta\mathrm{Ra}_{CB} > \Delta\mathrm{Ra}_{CB1}$) domains can be divided for the early stage. During this period, the effects of $\Delta\mathrm{Ra}_{CB}$ are coherent with theoretical predictions [15], and the critical value $\Delta\mathrm{Ra}_{CB1}$ is of the same order as the theoretical one $0.32\mathrm{Ra}_A$.

After this transition, each curve of l_m in Fig. 4 grows with time and finally reaches the bottom at t_e. It is found that t_e becomes smaller with increasing $\Delta\mathrm{Ra}_{CB}$, and another critical value $\Delta\mathrm{Ra}_{CB2} = 0.5\mathrm{Ra}_A$ appears. Beyond this value, fingering with chemical reaction arrives at the bottom earlier than its nonreactive counterpart. Similarly, the chemical stabilizing ($\Delta\mathrm{Ra}_{CB} < \Delta\mathrm{Ra}_{CB2}$) and destabilizing ($\Delta\mathrm{Ra}_{CB} > \Delta\mathrm{Ra}_{CB2}$) regions can be divided for the later fingering development stage. Note that this later-stage critical value $\Delta\mathrm{Ra}_{CB2}$ differs from the early stage $\Delta\mathrm{Ra}_{CB1}$. For the case with $\Delta\mathrm{Ra}_{CB1}$, dissolution-driven DI starts earlier, but generally slows down and finally reaches the bottom later than that in nonreactive Test NR. It can be explained by the fact that the nonlinear fingering growth and interactions at later times can slow down the vertical progression of dissolution-driven DI. In addition, the later-stage critical value $\Delta\mathrm{Ra}_{CB2}$, which is introduced by nonlinearities of fingering, has not been predicted by linear stability analysis [15].

It is noted that two critical values of $\Delta\mathrm{Ra}_{CB}$ are mainly introduced by the formation and development of density fingering, which may be influenced by the depth of porous media. To provide insights into this, three homogeneous media HO1–HO3 with different aspect ratios ($l_x/l_y =$ 2, 1, 2/3) are constructed and displayed in Fig. 5. These media share the same porosity and geometric size as medium HO in Fig. 1; namely, $l_x = 1$, $d = 12\delta_x$, $r_x = r_y = 27\delta_x$, and $l_p = 15\delta_x$. To focus on the effects of media length on two critical values of $\Delta\mathrm{Ra}_{CB}$, Test IV (see Table II) is then conducted in media HO1–HO3 separately. The simulation setup and parameters remain the same as in medium HO, but due to the change in aspect ratio, the grid sizes are set as $N_x \times N_y = 1500 \times 750$, 1500×1500, 1500×2250 for media HO1–HO3, respectively. The temporal evolutions of l_m are measured and illustrated in Fig. 6, and curves with larger $\Delta\mathrm{Ra}_{CB}$ are found to increase much faster. Besides, two critical values of $\Delta\mathrm{Ra}_{CB}$ can be observed in each of media HO1–HO3, and the early stage one is consistent with that in HO: $\Delta\mathrm{Ra}_{CB1} = 0.25\mathrm{Ra}_A$. However, the value of $\Delta\mathrm{Ra}_{CB2}$ for the late nonlinear period increases slightly with media depth: $\Delta\mathrm{Ra}_{CB2}/\mathrm{Ra}_A = 0.35,\ 0.35,\ 0.4$ for media HO1–HO3, respectively. It should be emphasized that, there is an increase of only 14% in the value

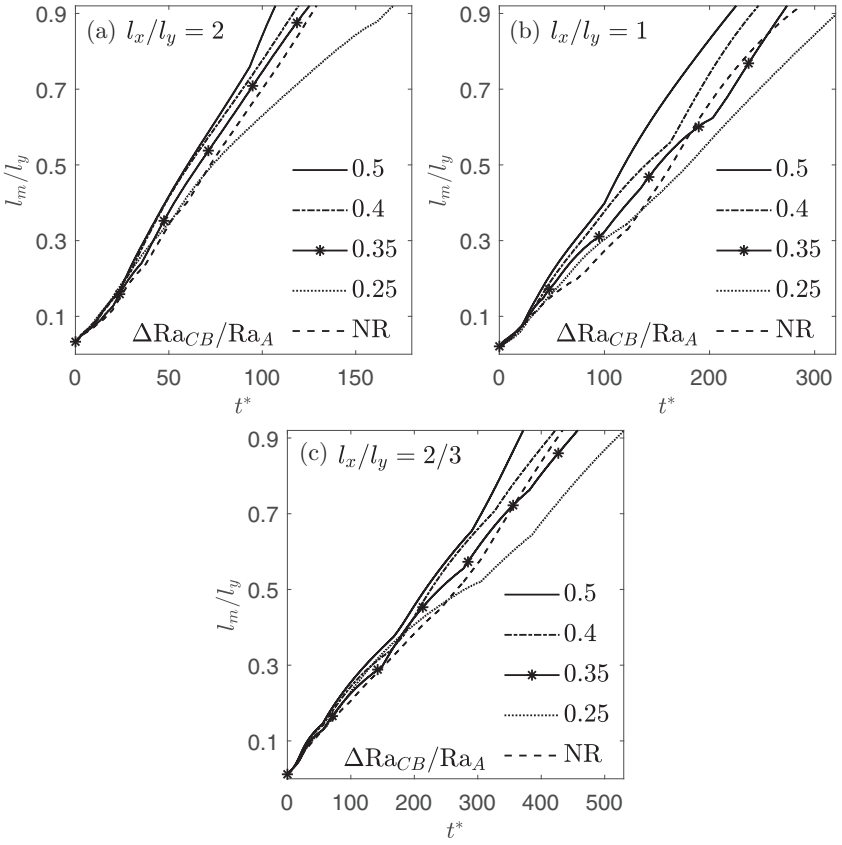

FIG. 6. Time evolutions of the mixing length for Test IV in homogeneous media HO1–HO3.

of $\Delta \mathrm{Ra}_{CB2}$, with the media length becoming 200% longer from HO1 to HO3. Therefore, the effects of $\Delta \mathrm{Ra}_{CB}$ in media HO1–HO3 show a similar tendency as in medium HO, and the influence of media depth on the two critical values of $\Delta \mathrm{Ra}_{CB}$ is not significant.

The simulated curves of l_m for Tests II and III are then analyzed as illustrated in Fig. 7. It is found that all reactive cases have smaller values of t_s and t_e compared with the nonreactive counterpart, and the difference is amplified when η [Fig. 7(a)] or Da [Fig. 7(b)] is larger. It implies that chemical reaction keeps accelerating the development of DI, while decreasing η or Da diminishes the destabilizing intensity. This feature is also suitable in the stabilizing group R1 with $\Delta \mathrm{Ra}_{CB} < 0$, and increasing η or Da can promote the stabilizing effects of the reaction. It can be concluded that increasing η or Da can enhance the influence of reaction $A + B \rightarrow C$ on the development of DI, but cannot significantly impact the stabilizing or destabilizing classification. On the contrary, increasing $\Delta \mathrm{Ra}_{CB}$ augments the destabilizing effects of chemistry, and subsequently features both stabilizing and destabilizing regimes. Thus the following parametric study focuses on the effects of $\Delta \mathrm{Ra}_{CB}$.

To better examine whether dissolution-driven DI returns to affect reaction $A + B \rightarrow C$, the volume-averaged reaction rate $\langle R^* \rangle$ is calculated. $\langle R^* \rangle$ reflects the global reaction strength, and the results for Test I are illustrated in Fig. 8. It is demonstrated that each profile of $\langle R^* \rangle$ evolves with time nonmonotonically at first and fluctuates around a steady-state value $\langle R^* \rangle_s$ after a while. $\langle R^* \rangle_s$ is limited by the steady-state mass flux J_s^* of species A from the top boundary as shown in Fig. 9(b). Regardless of the fluctuations, the global reaction rate $\langle R^* \rangle$ increases with $\Delta \mathrm{Ra}_{CB}$, and this can be expected since chemical reaction increasingly destabilizes the development of DI. To be specific, the stronger density fingering elongates the contact zone between two reactants A and B

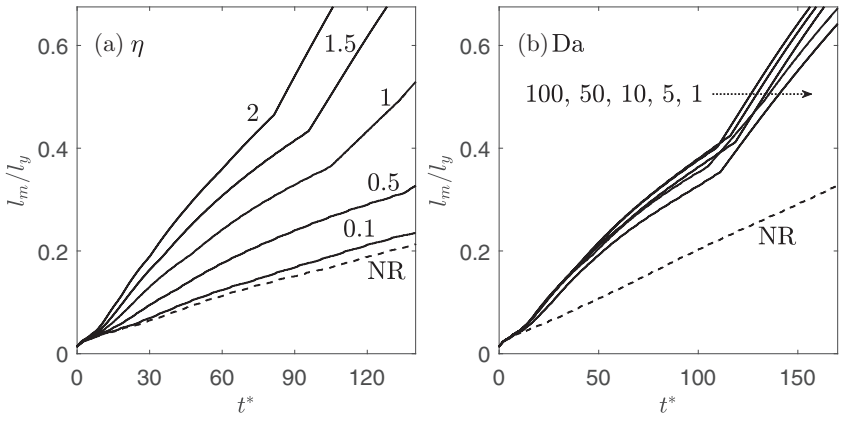

FIG. 7. Time evolution of the mixing length for Tests II and III in homogeneous medium HO.

more obviously, and in the mean time, the stronger convection brings reactant B up to react with species A more efficiently. The combination of the larger contact zone and local reaction rate leads to the increase of $\langle R^* \rangle$. Thus, dissolution-driven DI and reaction promote each other more strongly with increasing $\Delta \mathrm{Ra}_{CB}$ in the development process.

The dissolution of species A into the host fluid is always desirable in related industrial applications (like CO_2 sequestration). So, the effects of dissolution-driven DI with reaction $A + B \rightarrow C$ on the storage behavior of A are investigated. The horizontally averaged mass flux of species A at the top boundary is introduced as [30]

$$J^*(t) = -\frac{1}{l_x^* \sqrt{\mathrm{Ra}_A \mathrm{Sc}}} \int_0^{l_x^*} \partial_{y^*} C_A^*(x^*,\, 0) dx^*. \tag{37}$$

This parameter can be regarded as an indicator for the diffusing speed of species A into the host fluid. As illustrated in Fig. 9(a), the temporal evolution of J^* is qualitatively the same in both nonreactive and reactive cases. J^* initially decreases with time as long as diffusion dominates the transport process [Fig. 2, row (a)], then it starts to increase with the development of DI [Fig. 2, row (b)], after that it decreases again because of fingering merging [Figs. 2, rows (c) and (d)], and finally it

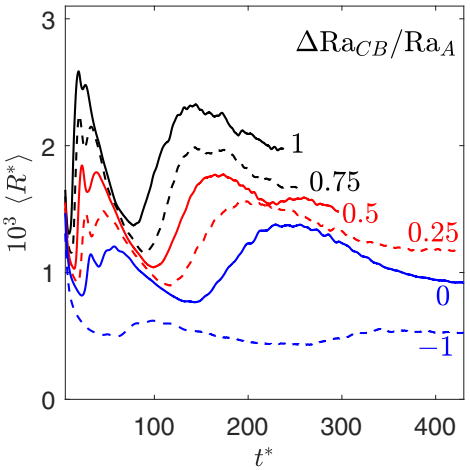

FIG. 8. Time evolution of the volume-averaged reaction rate for Test I in homogeneous medium HO.

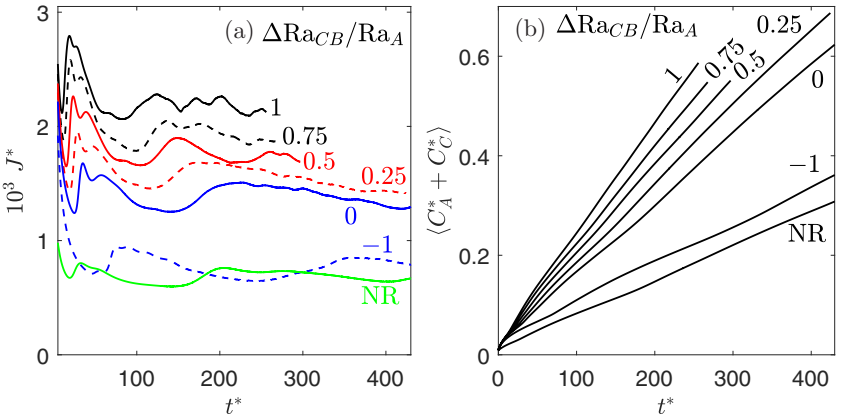

FIG. 9. Time evolution of the storage of species A for Test I in homogeneous medium HO.

fluctuates around a steady-state value J_s^* corresponding to the nearly unchanged number of fingers [Figs. 2, rows (e) and (f)]. Note that the later-stage fluctuations of J^* in Fig. 9(a) are introduced by the new fingering: J^* increases when new fingers form and decreases as they merge with existing ones. This behavior of J^* can verify the fingering promotion on the dissolution speed of species A. In addition, every reactive J^* is larger than the nonreactive counterpart, and the difference grows with ΔRa_{CB} [Fig. 9(a)]. It is because the chemical consumption of species A increases the concentration gradient $\partial_{y^*} C_A^*$ at the top boundary, and the larger ΔRa_{CB} leads to the stronger reaction intensity (Fig. 8).

To further quantify the storage behavior, the amount of A stored in the host fluid is also calculated. Considering the fact that species A can be stored in the form of either unreacted A or product C (reacted A), the stored A is defined as the volume-averaged concentration $\langle C_A^* + C_C^* \rangle$ [1]. As presented in Fig. 9(b), every curve of $\langle C_A^* + C_C^* \rangle$ increases with time monotonically. This can be explained by the evolution equation [1,31]

$$\frac{\partial \langle C_A^* + C_C^* \rangle}{\partial t^*} = l_x^* J^*, \tag{38}$$

which is obtained by integrating equations (15)–(17) over the whole spatial domain and taking into consideration the boundary conditions in Eq. (10). This equation expresses that $\langle C_A^* + C_C^* \rangle$ increases with time monotonically under different conditions, because the corresponding dissolution flux J^* in Fig. 9(a) remains positive. The results in Fig. 9(b) also demonstrate that all the reactive lines of $\langle C_A^* + C_C^* \rangle$ increase more quickly than the nonreactive one, implying the chemical promotion of the storage process, and this is introduced by the larger values of reactive J^* [Fig. 9(a)]. In addition, the growing speed of every reactive $\langle C_A^* + C_C^* \rangle$ in Fig. 9(b) increases with ΔRa_{CB}, which is consistent with the change of J^* in Fig. 9(a). Thus, the calculated J^* and $\langle C_A^* + C_C^* \rangle$ suggest that dissolution-driven DI with reaction can enhance the storage of species A in the host fluid, and the promotion extent increases with ΔRa_{CB}.

In general, a comprehensive parametric study of dissolution-driven DI with reaction $A + B \rightarrow C$ has been performed. The present pore-scale results about the effects of ΔRa_{CB} and η are qualitatively similar to previous theoretical predictions [15] and REV-scale findings [1]. During the later nonlinear growth period, however, the present critical value ΔRa_{CB2} to distinguish the stabilizing and destabilizing effects of chemistry is related to nonlinearities of fingering and has not been theoretically predicted by linear stability analysis [15]. In addition, the parameter Da is first investigated, and increasing Da amplifies the influence of chemistry.

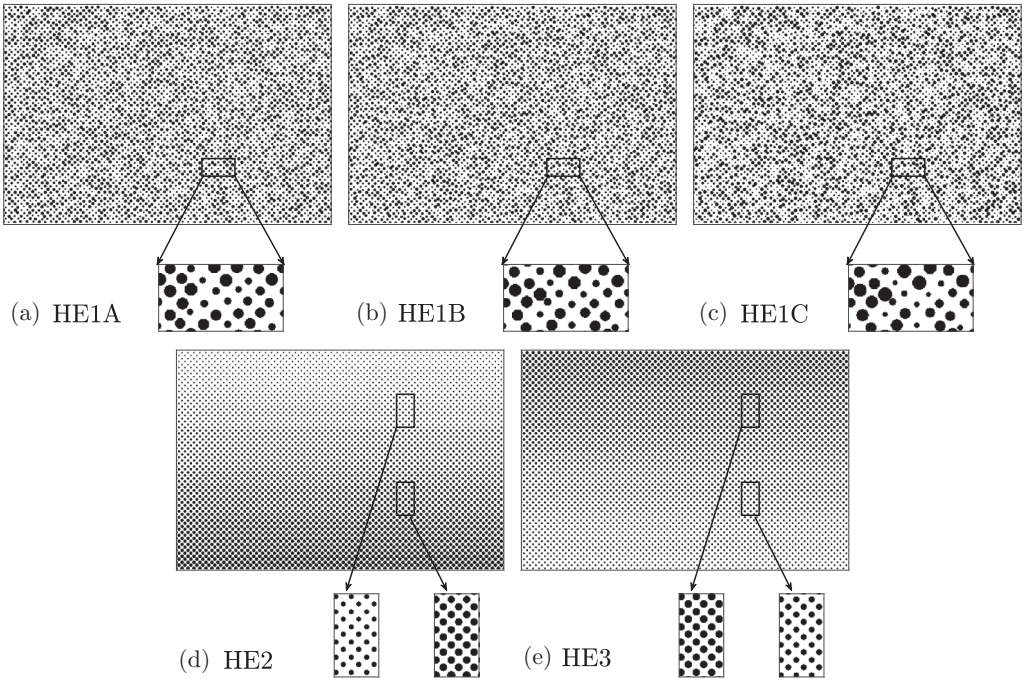

FIG. 10. Schematic diagrams of heterogeneous media HE1–HE3.

C. Media heterogeneity

Having investigated the dynamics of density fingering in homogeneous media, the effects of permeability anisotropy are further explored. As constructed in Fig. 10, three kinds of heterogeneous media (HE1–HE3) are considered. The random porous networks HE1, including HE1A–HE1C in Figs. 10(a)–10(c) are composed of randomly distributed circular grains with random diameters. In HE1, the spatial location of each grain center is first generated as in HO (Fig. 1), and then a random perturbation $(x_p,\ y_p)$ is added to each grain center in both horizontal and vertical directions as $G_{\mathrm{HE1}} = (x_c + x_p,\ y_c + y_p)$. Each grain diameter d is then randomly determined by [21]

$$d(\zeta) = \begin{cases} d_{\min}, & 0 \leqslant \zeta < \delta, \\ d_{\min} + \frac{d_{\max} - d_{\min}}{1-2\delta}(\zeta - \delta), & \delta \leqslant \zeta \leqslant 1-\delta, \\ d_{\max}, & 1-\delta < \zeta < \delta, \end{cases} \tag{39}$$

where ζ is a uniformly distributed random number within the interval $[0,\ 1]$. $d_{\min}$ and $d_{\max}$ are the minimum and maximum values of grain diameter, and δ is selected as 0.05. Related perturbations and grain diameters for media HE1A–HE1C are set as in Table III, and the mean grain diameter

TABLE III. Parameters for generating heterogeneous media HE1–HE3.

Media	Parameters
HE1A	$x_p(y_p) \in [-\delta_x,\ 4\delta_x],\ \ d_{\min} = 8\delta_x,\ \ d_{\max} = 16\delta_x$
HE1B	$x_p(y_p) \in [-2\delta_x,\ 2\delta_x],\ \ d_{\min} = 8\delta_x,\ \ d_{\max} = 16\delta_x$
HE1C	$x_p(y_p) \in [-\delta_x,\ 4\delta_x],\ \ d_{\min} = 6\delta_x,\ \ d_{\max} = 18\delta_x$
HE2	$d_t = 7\delta_x,\ \ l_{p,t} = 20\delta_x,\ \ \lambda = 0.01,\ \ r_x = r_y = 27\delta_x$
HE3	$d_t = 15\delta_x,\ \ l_{p,t} = 12\delta_x,\ \ \lambda = -0.006,\ \ r_x = r_y = 27\delta_x$

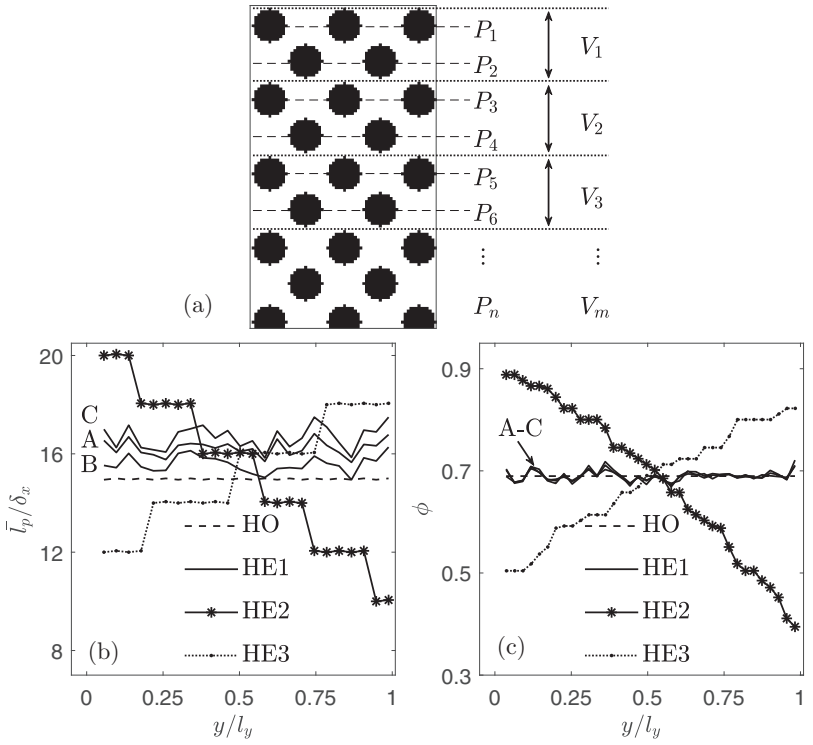

FIG. 11. (a) Measuring positions P_n and volumes V_m based on the structure of medium HO; (b), (c) Vertical evolution of horizontally averaged pore size and porosity in both homogeneous medium HO and heterogeneous media HE1–HE3.

in each medium is $12\delta_x$. On the other side, heterogeneous media HE2 and HE3 consist of regular circular grains with vertically decreasing (HE2) or increasing (HE3) pore spaces (permeability). The location of each grain center in these two media is also determined as in medium HO [$G_{\mathrm{HE2}} = G_{\mathrm{HE3}} = (x_c,\ y_c)$], and the vertical grain diameter gradient λ is calculated as

$$\lambda = \frac{d_b - d_t}{l_y}, \tag{40}$$

where d_b and d_t represent the grain diameters at bottom and top layers, respectively. Based on its definition, positive and negative values of λ correspond to media with decreasing (HE2) and increasing (HE3) pore spaces along the flow direction, respectively. Parameters for constructing media HE2 and HE3 [Figs. 10(d) and 10(e)] are provided in Table III. Considering that fingering mainly develops along the gravity field, the vertical change of horizontally averaged pore size $\bar{l}_p$ and porosity ϕ in both homogeneous and heterogeneous media are calculated. It should be emphasized that the measuring positions P_n for $\bar{l}_p$ and volumes V_m for ϕ are identical in each medium, and are all decided based on the porous structure of medium HO [see Fig. 11(a)]. The calculated results are illustrated in Figs. 11(b) and 11(c), and it is found that both $\bar{l}_p$ and ϕ decrease (increase) monotonically in medium HE2 (HE3) along the flow direction due to the change of grain diameters. On the other hand, in media HO and HE1A–HE1C, the calculated curves of ϕ remain nearly constant at 0.69 along the y direction, but the lines of $\bar{l}_p$ fluctuate around $15\delta_x$, $16\delta_x$, $15.5\delta_x$, and $16.5\delta_x$, respectively. Note that calculated results of $\bar{l}_p$ and ϕ in the three random media HE1A–HE1C show a similar tendency, and the values of $\bar{l}_p$ are all slightly larger than that in HO because of the random porous structures.

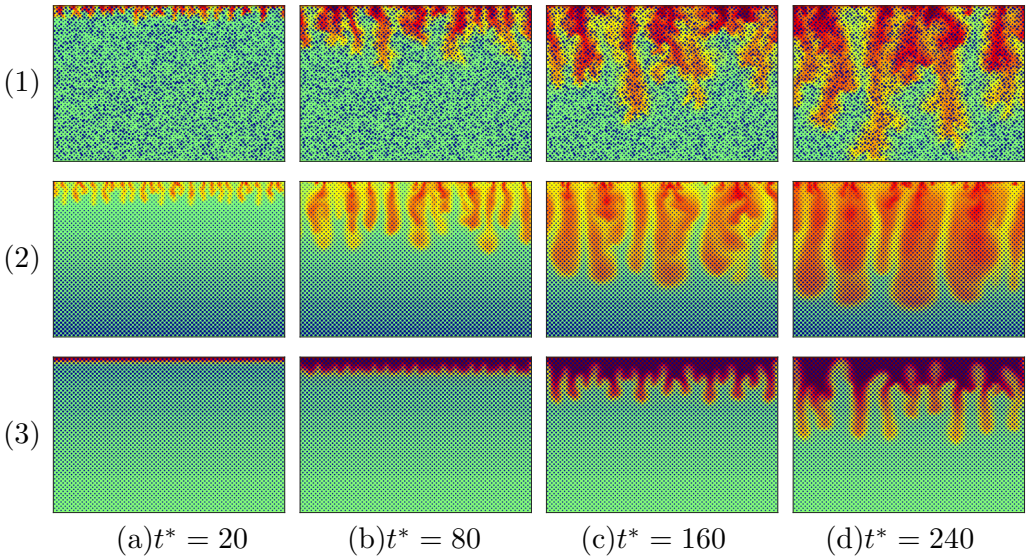

FIG. 12. Density fields for Test R2 in heterogeneous media HE1A–HE3.

Based on these heterogeneous media HE1–HE3, a series of simulation tests are performed, and the initial and boundary conditions are all set as in Eqs. (9) and (10). In agreement with the above homogeneous case HO, six types of dissolution-driven DI with reaction $A + B \rightarrow C$ can be observed in each heterogeneous medium. As an example, Fig. 12 portrays the density distributions in heterogeneous media for Test R2 (see Table I). Considering that the fingering characteristics in three random media HE1A–HE1C are similar to each other, Fig. 12, column (1) depicts only the density evolutions in HE1A. It is found that fingering growth in each heterogeneous medium experiences four similar stages as in HO [Fig. 2, column (3)], but the development details of density fingering are significantly influenced by the structure anisotropy. In medium HE1A, the large disorder in pore spaces promotes few fingers grow more rapidly and finally penetrate into the host fluid much deeper than the other fingers [Fig. 12, column (1)]. Besides, in medium HE1A, fingering tips are split by solid matrix regularly [Fig. 12, column (1)], and fingering interface becomes much rougher than that in HO (see outlines of density fingering in Fig. 13). In media HE2 and HE3 with regularly distributed matrix, however, fingering fronts show a relatively flat advancement, and fingering interface is smooth as in HO [see Figs. 12, column (2), 12, column (3), and 13]. In addition, compared with homogeneous case HO [Fig. 2, column (3)], fingers are much thicker in HE2 [Fig. 12, column (2)] while much thinner in HE3 [Fig. 12, column (3)], because of the vertical variation in pore spaces.

In addition to these various shapes of fingering, differences in advancing speed of fingering can also be observed from the calculated l_m in Fig. 14. It is found that density fingering in each of media HE1A–HE1C shows a similar tendency and develops at a nearly monotonic rate as in medium HO. In addition, among cases HO and HE1A–HE1C, fingering grows the fastest in HE1C and the slowest

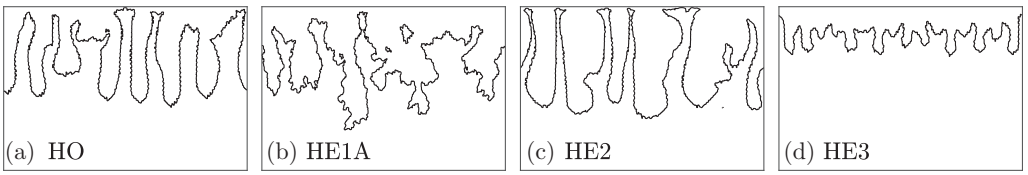

FIG. 13. Outlines of density fingering in both homogeneous medium HO and heterogeneous media HE1A–HE3 at $t^* = 160$.

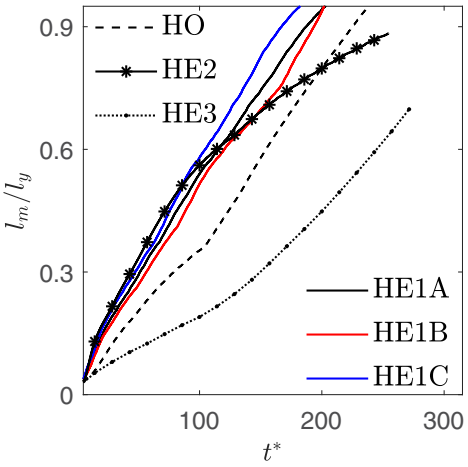

FIG. 14. Time evolution of the mixing length for Test R2 in both homogeneous medium HO and heterogeneous media HE1–HE3.

in HO. This is reasonable since, in these four media, the values of ϕ are nearly unchanged along the flow direction [Fig. 11(c)], but $\bar{l}_p$ has the largest (smallest) value in HE1C (HO) [Fig. 11(b)], suggesting the promotion effects of large pore size on fingering growth. For media HE2 and HE3 however, the calculated curves of l_m exhibit two successive different velocities, which differs from the homogeneous case HO obviously. This can also be explained by the change of pore size and porosity along the flow direction [Figs. 11(b) and 11(c)]. In HE2, the large pore bodies near the top boundary exert small resistance and help fingering grow the fastest among the four media at first. Then the development of fingering in HE2 is gradually suppressed by the increasingly large resistance along the flow direction and finally becomes slower than the homogeneous case HO. On the contrary, density fingering in HE3 develops with a totally converse trend, since the permeability is reversed to increase vertically. That is, initially, the fluid interface is nearly stable with much weak density fingering and fingering becomes obvious and develops fast after a while. Note that density fingering still develops the slowest in HE3 among the six cases, even though its growing speed increases in later stages.

To quantitatively characterize the effects of media heterogeneity on the storage efficiency, two metrics J^* and $\langle C_A^* + C_C^* \rangle$ are calculated. In Fig. 15(a), the time evolutions of mass flux J^* are presented for analysis. It is found that J^* fluctuates and finally collapses to a steady-state value in each of media HE1A–HE1C, which is consistent with its homogeneous counterpart. This is introduced by their similar distributions of pore size and porosity along the flow direction [Figs. 11(b) and 11(c)]. In media HE2 and HE3, however, curves of J^* deviate from the homogeneous case significantly. To be specific, in medium HE2, J^* initially shows a similar fashion as that in HO, but it keeps decreasing at later stage due to the reduction of pore spaces along the flow direction. In medium HE3, J^* deviates from the homogeneous case after the initial decrease stage, and it remains almost constant because of the significant suppression of porous structure on fingering development. The calculated profiles of $\langle C_A^* + C_C^* \rangle$ are also plotted in Fig. 15(b), and all these curves increase with time in a similar fashion, which can be expected by Eq. (38). In addition, the calculated lines of $\langle C_A^* + C_C^* \rangle$ in HO and HE1A–HE1C are nearly identical, implying that these four media have a storage capacity similar to that of species A. It should be emphasized that both J^* and $\langle C_A^* + C_C^* \rangle$ become larger in HE2 but smaller in HE3 than those in HO, suggesting that medium HE2 can enhance the diffusion of A into the host fluid.

Fingering in each of media HE1A–HE1C develops faster than that in HO [Fig. 11(b)], but the storage behavior of species A is nearly identical in these four media (Fig. 15). To further examine

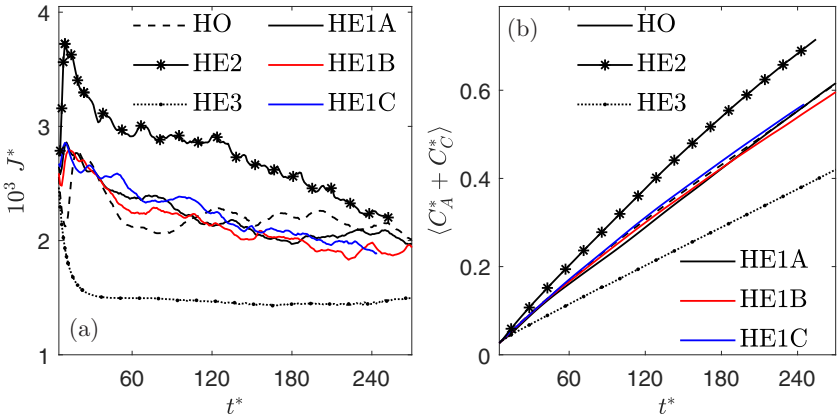

FIG. 15. Time evolution of the storage of species A for Test R2 in both homogeneous medium HO and heterogeneous media HE1–HE3.

the differences between fingering characteristics in homogeneous and random heterogeneous media, two homogeneous media HOA and HOB are generated as in Fig. 16. The pore sizes in HOA and HOB are selected as the largest and smallest ones in medium HE1A, which have been calculated as $24.4\delta_x$ and $6\delta_x$, respectively. In media HOA and HOB, solid grains also obey a staggered distribution as in HO, but geometric parameters become $d = 19.5\delta_x$, $r_x = r_y = 43.9\delta_x$, $l_p = 24.4\delta_x$ for medium HOA, and $d = 4.8\delta_x$, $r_x = r_y = 10.8\delta_x$, $l_p = 6\delta_x$ for medium HOB. Note that the number of grains in these two media are different from that in HO, but their porosity and computational domain remain the same. Besides, it is obtained by calculation that, in media HOA and HOB, ϕ remains almost constant as 0.69 along the y direction, and $\bar{l}_p$ fluctuates around $24.4\delta_x$ and $6\delta_x$, respectively. Thus, the vertical changes of ϕ in media HOA and HOB are similar to those in HE1A–HE1C. But the values of $\bar{l}_p$ along the flow direction in HE1A–HE1C are bounded by those in HOA and HOB. Based on media HOA and HOB, Test R2 is carried out separately, and temporal evolutions of l_m, J^*, and $\langle C_A^* + C_C^* \rangle$ are calculated and compared with the corresponding results in HE1A–HE1C. As displayed in Fig. 17, among the five cases, fingering develops the fastest and the largest amount of species A can be stored in HOA that with the largest pore size. In addition, the simulated results in media HE1A–HE1C are all bounded by those in HOA and HOB, which is consistent with their vertical distributions of $\bar{l}_p$. These results demonstrate that fingering characteristics in heterogeneous media HE1 can deviate from the homogeneous case obviously by changing their

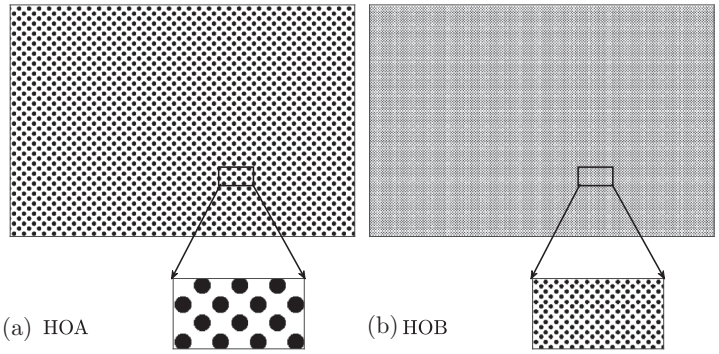

FIG. 16. Schematic diagram of homogeneous media HOA-HOB with different pore sizes.

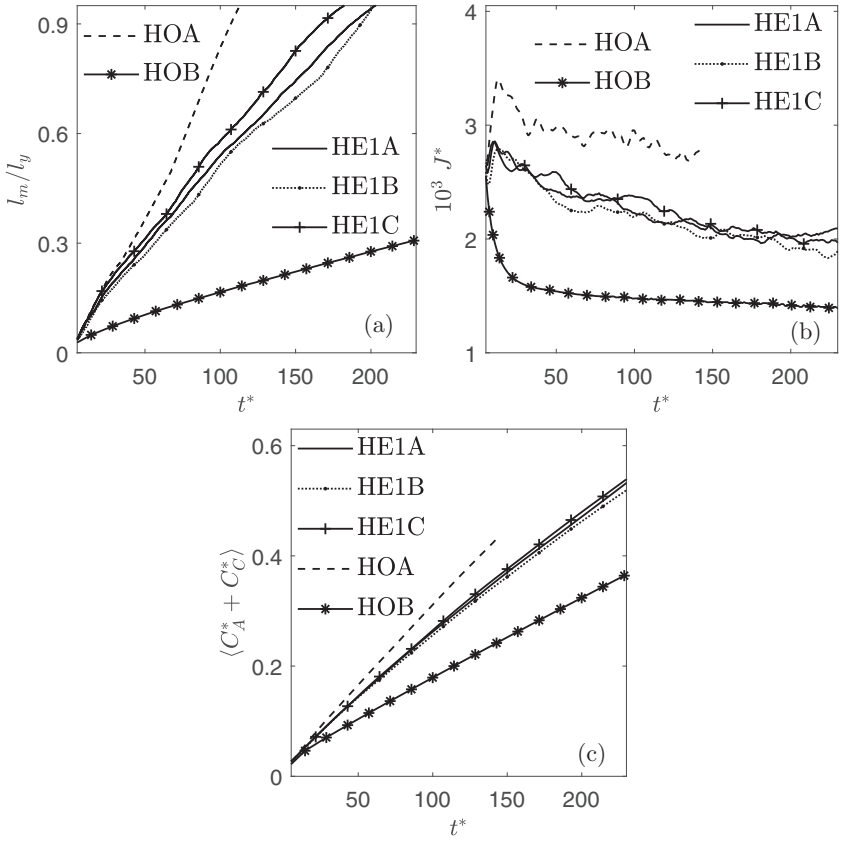

FIG. 17. Time evolution of the mixing length and the storage of species A for Test R2 in both homogeneous media HOA and HOB and heterogeneous media HE1A–HE1C.

pore size distributions. In addition, they also verify the above argument that a medium with large pore size is favorable for fingering development and storage of species A.

In summary, simulations have been conducted in three kinds of heterogeneous media, and reaction $A + B \rightarrow C$ can introduce six types of fingering scenarios, which is similar to the aforementioned homogeneous cases. Besides, the medium heterogeneity can influence the advancing position, shape, and speed of density fingering. In terms of the storage efficiency of species A, the calculated $\langle C_A^* + C_C^* \rangle$ and J^* indicate that medium HE2 with large pore spaces in the top area is favorable.

V. CONCLUSIONS

In this work, a series of pore-scale simulations about dissolution-driven DI with reaction $A + B \rightarrow C$ in porous media are carried out based on a MRT LB model. One homogeneous medium and three types of heterogeneous media HE1–HE3 are artificially constructed, with HE1A–HE1C having randomly distributed solid grains and HE2 and HE3 having vertically decreasing (HE2) or increasing (HE3) pore spaces. These media share the same porosity and computational domain.

The results in homogeneous media have provided two nonreactive and four reactive types of fingering scenarios and have suggested that reactions can enhance, refrain, or even trigger the development of dissolution-driven DI. Then, a parametric study has demonstrated that increasing $\Delta \mathrm{Ra}_{CB}$ can introduce stronger density fingering and reaction, improve the storage of A, and also realize the transition from stabilizing to destabilizing scenarios. In addition, increasing η and/or Da

can intensify the influence of chemistry on DI, without influencing the stabilizing or destabilizing classification. These results can qualitatively confirm existing theoretical predictions and REV-scale simulations. Note that, for some intermediate $\Delta \mathrm{Ra}_{CB}$, fingering with reaction may start earlier but progressively become slower than its nonreactive counterpart, and this is introduced by later-stage nonlinearities and has not been predicted by linear stability analysis. In addition, differences between the present pore-scale and existing REV-scale density profiles have also been observed, which can be explained by the over-prediction of reaction intensity on REV scale.

A series of simulations have been carried out in heterogeneous media to further explore the effects of medium anisotropy. Numerical results have showed that the inclusion of reaction $A + B \rightarrow C$ can introduce six types of dissolution-driven DI as the homogeneous case, but the medium heterogeneity can significantly affect the development details. Compared with the homogeneous case, media HE1A–HE1C can introduce obvious tip-splitting phenomena and rougher fingering interfaces, and media HE2 and HE3 can produce smooth but much thicker or thinner fingering. As for the growing speed, fingering develops the fastest in HE1C, and the slowest in HE3. Besides, in medium HE2, fingering grows faster in early times, but finally becomes slower than the homogeneous case, because it is gradually suppressed by the vertical reduction of permeability. In terms of the storage behavior of species A, three random media HE1A–HE1C show a similar capacity as the homogeneous one, and medium HE2 with large pore spaces near the top boundary can introduce intensive diffusion of species A into the host fluid.

These pore-scale results have provided insights into dissolution-driven DI with reaction $A + B \rightarrow C$, and are important in related applications. For example, in the context of CO_2 sequestration, enhancing the dissolution of CO_2 is crucial to improving the storage efficiency and safety. The classified different types of DI can provide a method to compare different geological storage sites according to their chemical compositions and select those where reactions can help in destabilizing density fingering and accelerating the storage of CO_2. Besides, the effects of porous heterogeneity have highlighted the criterion that media with random structure or large pore size in the top layer can be selected in related applications depending on their desired instability behavior: deeper advancing position or more intensive storage of species A.

ACKNOWLEDGMENTS

This work was supported by the UK Engineering and Physical Sciences Research Council under the project "UK Consortium on Mesoscale Engineering Sciences (UKCOMES)" (Grants No. EP/L00030X/1 and No. EP/R029598/1), and the China Scholarship Council (CSC) under Grant No. 201706160161.

[1] V. Loodts, B. Knaepen, L. Rongy, and A. De Wit, Enhanced steady-state dissolution flux in reactive convective dissolution, Phys. Chem. Chem. Phys. **19**, 18565 (2017).

[2] R. A. Wooding, S. W. Tyler, and I. White, Convection in groundwater below an evaporating salt lake: 1. Onset of instability, Water Resour. Res. **33**, 1199 (1997).

[3] J. D. Stevens, J. M. Sharp, C. T. Simmons, and T. R. Fenstemaker, Evidence of free convection in groundwater: Field-based measurements beneath wind-tidal flats, J. Hydrol. (Amsterdam, Neth.) **375**, 394 (2009).

[4] L. Rongy, K. B. Haugen, and A. Firoozabadi, Mixing from Fickian diffusion and natural convection in binary non-equilibrium fluid phases, AIChE J. **58**, 1336 (2012).

[5] M. A. Budroni, C. Thomas, and A. De Wit, Chemical control of dissolution-driven convection in partially miscible systems: Nonlinear simulations and experiments, Phys. Chem. Chem. Phys. **19**, 7936 (2017).

[6] M. A. Budroni, L. A. Riolfo, L. Lemaigre, F. Rossi, M. Rustici, and A. De Wit, Chemical control of hydrodynamic instabilities in partially miscible two-layer systems, J. Phys. Chem. Lett. **5**, 875 (2014).

[7] C. Wylock, A. Rednikov, B. Haut, and P. Colinet, Nonmonotonic Rayleigh-Taylor instabilities driven by gas-liquid CO_2 chemisorption, J. Phys. Chem. B **118**, 11323 (2014).

[8] C. Wylock, A. Rednikov, P. Colinet, and B. Haut, Experimental and numerical analysis of buoyancy-induced instability during CO_2 absorption in $NaHCO_3$-Na_2CO_3 aqueous solutions, Chem. Eng. Sci. **157**, 232 (2017).

[9] C. Thomas, V. Loodts, L. Rongy, and A. De Wit, Convective dissolution of CO_2 in reactive alkaline solutions: Active role of spectator ions, Int. J. Greenhouse Gas Control **53**, 230 (2016).

[10] I. Cherezov and S. S. S. Cardoso, Acceleration of convective dissolution by chemical reaction in a Hele-Shaw cell, Phys. Chem. Chem. Phys. **18**, 23727 (2016).

[11] C. Thomas, L. Lemaigre, A. Zalts, A. D'Onofrio, and A. De Wit, Experimental study of CO_2 convective dissolution: The effect of color indicators, Int. J. Greenhouse Gas Control **42**, 525 (2015).

[12] M. C. Kim, Effect of the irreversible $A + B \rightarrow C$ reaction on the onset and the growth of the buoyancy-driven instability in a porous medium, Chem. Eng. Sci. **112**, 56 (2014).

[13] M. C. Kim and C. Wylock, Linear and nonlinear analyses of the effect of chemical reaction on the onset of buoyancy-driven instability in a CO_2 absorption process in a porous medium or Hele-Shaw cell, Can. J. Chem. Eng. **95**, 589 (2017).

[14] V. Loodts, C. Thomas, L. Rongy, and A. De Wit, Control of Convective Dissolution by Chemical Reactions: General Classification and Application to CO_2 Dissolution in Reactive Aqueous Solutions, Phys. Rev. Lett. **113**, 114501 (2014).

[15] V. Loodts, L. Rongy, and A. De Wit, Chemical control of dissolution-driven convection in partially miscible systems: Theoretical classification, Phys. Chem. Chem. Phys. **17**, 29814 (2015).

[16] V. Loodts, P. M. J. Trevelyan, L. Rongy, and A. De Wit, Density profiles around $A + B \rightarrow C$ reaction-diffusion fronts in partially miscible systems: A general classification, Phys. Rev. E **94**, 043115 (2016).

[17] P. Cheng, M. Bestehorn, and A. Firoozabadi, Effect of permeability anisotropy on buoyancy-driven flow for CO_2 sequestration in saline aquifers, Water Resour. Res. **48**, W09539 (2012).

[18] Z. L. Guo and C. Shu, *Lattice Boltzmann method and its Applications in Engineering* (World Scientific Publishing Company, Singapore, 2013), pp. 25–28, 76–78, 329–338.

[19] Q. Li, K. H. Luo, Q. J. Kang, Y. L. He, Q. Chen, and Q. Liu, Lattice Boltzmann methods for multiphase flow and phase-change heat transfer, Prog. Energy Combust. Sci. **52**, 62 (2016).

[20] T. M. Lei, X. H. Meng, and Z. L. Guo, Pore-scale study on reactive mixing of miscible solutions with viscous fingering in porous media, Comput. Fluids **155**, 146 (2017).

[21] H. H. Liu, Y. H. Zhang, and A. J. Valocchi, Lattice Boltzmann simulation of immiscible fluid displacement in porous media: Homogeneous versus heterogeneous pore network, Phys. Fluids **27**, 052103 (2015).

[22] C. Chen and D. Zhang, Pore-scale simulation of density-driven convection in fractured porous media during geological CO_2 sequestration, Water Resour. Res. **46**, W11527 (2010).

[23] Z. L. Guo and C. G. Zheng, Analysis of lattice Boltzmann equation for microscale gas flows: Relaxation times, boundary conditions and the Knudsen layer, Int. J. Comput. Fluid Dyn. **22**, 465 (2008).

[24] X. H. Meng and Z. L. Guo, Multiple-relaxation-time lattice Boltzmann model for incompressible miscible flow with large viscosity ratio and high Peclet number, Phys. Rev. E **92**, 043305 (2015).

[25] C. X. Pan, L. S. Luo, and C. T. Miller, An evaluation of lattice Boltzmann schemes for porous medium flow simulation, Comput. Fluids **35**, 898 (2006).

[26] A. J. C. Ladd, Numerical simulations of particulate suspensions via a discretized Boltzmann equation. Part 1. Theoretical foundation, J. Fluid Mech. **271**, 285 (1994).

[27] A. J. C. Ladd, Numerical simulations of particulate suspensions via a discretized Boltzmann equation. Part 2. Numerical Results, J. Fluid Mech. **271**, 311 (1994).

[28] A. M. Tartakovsky, G. D. Tartakovsky, and T. D. Scheibe, Effects of incomplete mixing on multicomponent reactive transport, Adv. Water Resour. **32**, 1674 (2009).

[29] A. M. Tartakovsky and S. P. Neuman, Effects of Peclet number on pore-scale mixing and channeling of a tracer and on directional advective porosity, Geophys. Res. Lett. **35**, L21401 (2008).

[30] P. Ghoshal, M. C. Kim, and S. S. S. Cardoso, Reactive-convective dissolution in a porous medium: The storage of carbon dioxide in saline aquifers, Phys. Chem. Chem. Phys. **19**, 644 (2017).

[31] J. J. Hidalgo, J. Fe, L. Cueto-Felgueroso, and R. Juanes1, Scaling of Convective Mixing in Porous Media, Phys. Rev. Lett. **109**, 264503 (2012).